Pergamon

J. Mech. Phys. Solids, Vol. 44, No. 5, pp. 751–769, 1996

0022–5096/96 $15.00+0.00

PII S0022-5096(95)00026-9

RELIABILITY OF CERAMIC MULTILAYER ACTUATORS: A NONLINEAR FINITE ELEMENT SIMULATION

X. GONG and Z. SUO

Mechanical and Environmental Engineering Department, Materials Department, University of California, Santa Barbara, CA 93106, U.S.A.

ABSTRACT

In a ceramic multilayer actuator, the abrupt end of an internal electrode concentrates the electric field, inducing stresses in the ceramic. Crack nucleation and growth have been observed experimentally, but have not been well modeled due to the complex material behaviors. We write a finite element program to solve this coupled electromechanical problem. The material is taken to be nonlinearly dielectric with electrostrictive strain quadratic in electric displacement. The program solves field distributions in a multilayer actuator, which are combined with fracture mechanics to obtain cracking condition. The calculations are compared with the existing analytical solution under the small-scale saturation conditions, and then extended to the large-scale saturation conditions. We show that the cracking condition established under the small-scale saturation conditions gives useful estimate even when the saturation zone is comparable to the actuator layer thickness.

1. INTRODUCTION

Ceramic multilayer actuators have found a wide range of applications owing to their small volumes, quick response, low energy consumption, and large generative forces (Uchino, 1993; Rogers, 1995). Various electrode configurations have been proposed (Yoshikawa and Shrout, 1993), one of which is shown in Fig. 1. An actuator often

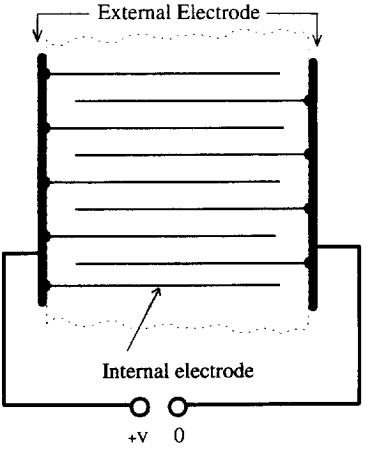

Fig. 1. A schematic picture of ceramic multilayer actuator.

consists of hundreds of ceramic layers, alternating with thin metal films (internal electrodes). Each metal film connects one edge to one of the external electrode strips, and terminates another edge inside the ceramic to maintain insulation. The terminated electrode edges raise a serious reliability problem. Cracks start in the ceramic around the electrode edges, grow and damage the device (Furuta and Uchino, 1993; Aburatani *et al.*, 1994; Schneider *et al.*, 1994).

Figure 2 illustrates a basic cracking mechanism (Suo, 1993). When a voltage V is applied to the multilayer actuator, an electric field $E_{\text{appl}} = V/H$ prevails in the region covered by two internal electrodes, where H is the individual ceramic layer thickness [Fig. 2(a)]. However, the electric field around a terminated electrode edge is non-uniform and much higher than E_{appl} [Fig. 2(b)]. Consequently, the ceramic around the electrode edge undergoes an incompatible deformation due to either ferroelectric switching or electrostriction [Fig. 2(c)]. The incompatible deformation, in its turn, induces a stress field that may activate flaws in the ceramic to grow.

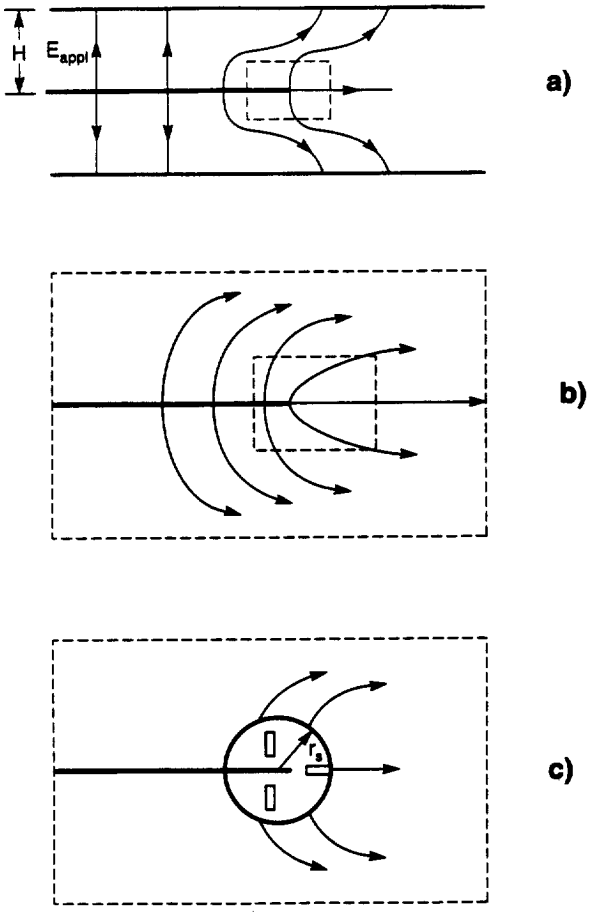

Fig. 2. A basic mechanism for cracking around an electrode edge.

Winzer *et al.* (1989) was the first to analyze the problem using finite element method. They determined the electric field in an actuator assuming that the ceramic is linearly dielectric, and then solved a linear elastic problem to determine the stress field induced by quadratic electrostriction. Yang and Suo (1994) studied the similar problems analytically, and showed that at a small distance r from an internal electrode edge, the stress field is $1/r$ singular. The strong singularity results from two idealizations: the electrode was taken to be a mathematical plane with no thickness, and the ceramic was linearly dielectric. In reality, as the electric field increases, the electric displacement saturates, resulting in a lower electrostrictive strain than that predicted from a linear dielectric. Yang and Suo (1994) proposed a step-like electrostriction model, and showed that the stress is no longer singular. For an electrostrictive ceramic with saturated electric displacement, Hom and Shankar (1995) and Hao *et al.* (1996) showed that the stress field around the electrode edge is only logarithmic singular.

The analytical solutions are only valid under the small-scale saturation conditions, and are obtained under the condition that the stress field does not affect the electric field. To analyze the problem, with realistic device geometries and nonlinear electromechanical coupling, one has to write a finite element program (Gong, 1994, 1995). Independent of our work, Hom and Shankar (1995) have formulated a finite element approach to the same problem. Their formulation differs from ours, but the two formulations give similar numerical results. The present paper builds upon the previous work and reports details of a finite element simulation. The conclusion is expected to be useful in actuator design. Section 2 formulates the coupled electromechanical field in a ceramic multilayer actuator as a boundary value problem. This problem is then solved by a finite element method outlined in Appendix A. Section 3 reviews the small-scale saturation model, and compares the solution with the finite element results. Section 4 extends the finite element analysis to the actuators under large-scale saturation conditions.

2. PROBLEM FORMULATION

We focus our attention on plane strain problems, which allow us to compare finite element results with existing analytical solutions. This section lists governing equations and boundary conditions for an actuator. Details of the finite element formulation specific to nonlinear electrostrictive ceramics are given in Appendix A. Once the stress field is solved, we apply fracture mechanics to obtain the stress intensity factor.

2.1. *Governing equations*

Subject a solid dielectric to a distribution of displacements u, v in the x, y directions, and electric potential ϕ. The strain tensor, γ, and the electric field vector $\mathbf{E}$, are the gradients

$$\gamma_{ij} = \tfrac{1}{2}(u_{i,j}+u_{j,i}), \quad E_i = -\phi_{,i}. \tag{2.1}$$

Across an interface, the stress tensor, $\boldsymbol{\sigma}$, and the electric displacement vector, $\mathbf{D}$, jump by

$$n_i[\sigma_{ij}^+ - \sigma_{ij}^-] = t_j, \quad n_i[D_i^+ - D_i^-] = -\omega, \tag{2.2}$$

where **n** is the unit vector normal to the interface pointing from the − side to the + side, **t** is the traction, and ω is the charge per unit area, externally applied on the interface. If the material is free of space charge and body force, the stress tensor and the electric displacement vector are divergence-free, namely,

$$\sigma_{ij,j} = 0, \quad D_{i,i} = 0. \tag{2.3}$$

Suo (1991), and Hom and Shankar (1994) proposed a set of constitutive equations for nonlinear, isotropic electrostrictive ceramics on the basis of experimental observations and thermodynamic considerations. Under the plane strain conditions, the constitutive equations take the form

$$\gamma_{xx} = [(1-\nu^2)\sigma_{xx} - \nu(1+\nu)\sigma_{yy}]/Y + Q[(1-\nu q)D_x^2 - q(1+\nu)D_y^2] \tag{2.4a}$$

$$\gamma_{yy} = [(1-\nu^2)\sigma_{yy} - \nu(1+\nu)\sigma_{xx}]/Y + Q[(1-\nu q)D_y^2 - q(1+\nu)D_x^2] \tag{2.4b}$$

$$\gamma_{xy} = (1+\nu)\sigma_{xy}/Y + Q(1+q)D_xD_y \tag{2.4c}$$

$$E_x = -2Q[(1-\nu q)D_x\sigma_{xx} + (1+q)D_y\sigma_{xy} - q(1+\nu)D_x\sigma_{yy} - q^2D_xYQ(D_x^2+D_y^2)] + f(D)D_x/D \tag{2.4d}$$

$$E_y = -2Q[(1-\nu q)D_y\sigma_{yy} + (1+q)D_x\sigma_{xy} - q(1+\nu)D_y\sigma_{xx} - q^2D_yYQ(D_x^2+D_y^2)] + f(D)D_y/D. \tag{2.4e}$$

Here $D = (D_iD_i)^{1/2}$ is the magnitude of the electric displacement, ν is Poisson's ratio, Y is Young's modulus, Q and q are the electrostrictive coefficients. The strains are linear in the stresses (elasticity) and quadratic in the electric displacements (electrostriction). The electric field is nonlinear in electric displacements (dielectric effects), and also depends on stresses (converse electrostrictive effects). The function, $E = f(D)$, is the dielectric response in the absence of stress. Experiments have shown that when the electric field increases, its ability to induce further electric displacement decreases, which finally saturates at a constant value D_s (Uchino and Nomura, 1983; Jang *et al.*, 1989; Cao and Evans, 1993; Lynch *et al.*, 1994; Lynch, 1995).

Figure 3 shows two D–E relations in the absence of stress. The relation used by Gong (1994), Hom and Shankar (1994) and Gong (1995) in the finite element analysis is written as

$$f(D) = \frac{E_s}{2}\ln\left(\frac{1+D/D_s}{1-D/D_s}\right). \tag{2.5}$$

Here D_s is the saturated electric displacement, E_s is a characteristic electric field. When E is small, D is linearly proportional to E, and the slope defines the dielectric permittivity ε. One can confirm that

$$E_s = D_s/\varepsilon. \tag{2.6}$$

The solid line in Fig. 3 is the D–E relation used by Hao *et al.* (1996). When $E < E_s$, the ceramic is linear. When $E > E_s$, D is maintained at the constant saturation value

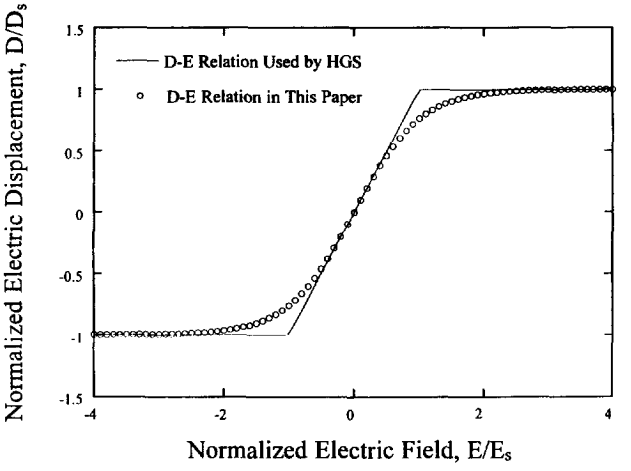

Fig. 3. The electric field and electric displacement relations used in the HGS solution and in this paper for finite element analysis.

D_s. The relationship (2.6) among the three parameters D_s, E_s and ε is the same for the two dielectric laws.

Notice that when the electric displacement saturates, the electrostrictive strain also saturates. This introduces another important parameter in actuator design

$$\gamma_s = QD_s^2, \tag{2.7}$$

which is the saturation strain along the electric field direction in the absence of stress. The saturation strain transverse to the electric field is $-qQD_s^2$.

2.2. *Boundary conditions*

Figure 4 shows the boundary conditions appropriate for a multilayer actuator. Place the origin of the Cartesian coordinate x–y at a terminated electrode edge. Because of the symmetry, only half of an individual layer needs to be analyzed. Along the upper electrode, the vertical displacement is constant

$$v(x, H) = \text{constant}. \tag{2.8a}$$

The value of the constant is to be determined as a part of the solution. The electric field potential equals the applied electric voltage,

$$\phi(x, H) = V_{\text{appl}}. \tag{2.8b}$$

When no external stress is applied on the actuator, the shear stress and the vertical resultant force vanish, namely

$$\sigma_{xy} = 0, \quad \int_{-L_2}^{L_1} \sigma_{yy}(x, H)\,\mathrm{d}x = 0. \tag{2.8c}$$

The lower electrode is connected to the ground, so that

$$\phi(x, 0) = 0, \quad -L_2 \leqslant x \leqslant 0. \tag{2.8d}$$

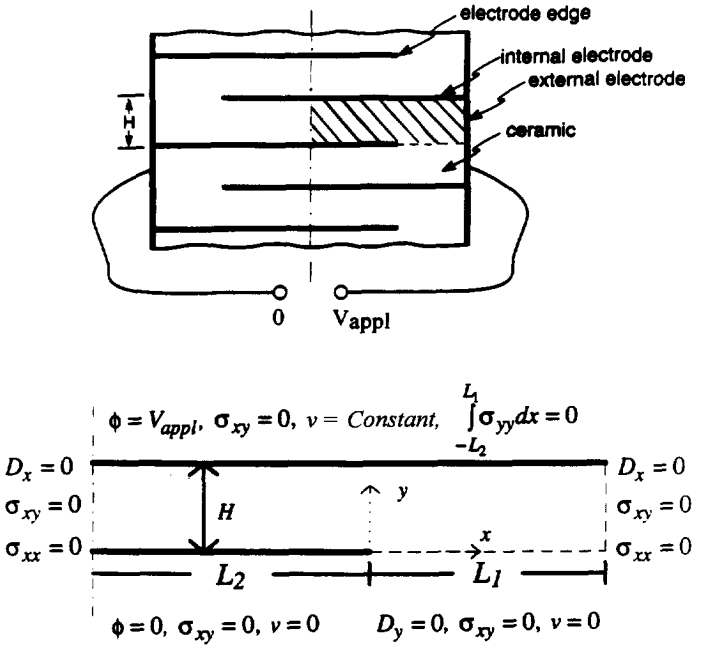

Fig. 4. Boundary conditions for a multilayer actuator.

The vertical displacement and the shear stress vanish on both the electrode and its front plane due to the symmetry

$$v(x, 0) = 0, \quad \sigma_{xy} = 0, \quad -L_2 \leqslant x \leqslant L_1. \tag{2.8e}$$

In front of the lower electrode plane, due to symmetry, the vertical electric displacement vanishes

$$D_y(x, 0) = 0, \quad 0 < x < L_1. \tag{2.8f}$$

At the end of the actuator and its vertical symmetric plane, tractions and horizontal electric displacement vanish

$$\sigma_{xx} = 0, \quad \sigma_{xy} = 0, \quad D_x = 0. \tag{2.8g}$$

To avoid rigid body motion, we constrain the horizontal motion at the left lower corner

$$u(-L_2, 0) = 0. \tag{2.8h}$$

2.3. *Stress far away from the electrode edge*

We will use finite element program to analyze a special case that both L_1 and L_2 are much larger than H. Although this configuration is different from a typical actuator, it emphasizes the conditions around the electrode edge with minimum complications from the external boundaries. The more realistic complication $L_1 \ll L_2$, $L_1 \approx H$ will be studied elsewhere.

When $L_1 \gg H$ and $L_2 \gg H$, one can readily determine the stresses in the actuator far away from the electrode, where the electric field is uniform, vanishing in the inactive part and equal to the applied electric field in the active part. The only nonzero stress component is σ_{yy}, which is tensile ahead of the electrode edge, and compressive behind, due to the global mismatch between the active part and the inactive part. Denote the stress far ahead of the electrode edge by σ^+ and the stress far behind the electrode edge by σ^-. The resultant force vanishes

$$L_1\sigma^+ + L_2\sigma^- = 0. \tag{2.9a}$$

The vertical displacement is the same in both parts

$$\frac{1-v^2}{Y}\sigma^- + (1-vq)QD^2 = \frac{1-v^2}{Y}\sigma^+. \tag{2.9b}$$

These two equations solve the two stresses, giving

$$\sigma^+ = \frac{L_2}{L_1+L_2}\frac{1-vq}{1-v^2}YQD^2, \tag{2.10a}$$

$$\sigma^- = -\frac{L_1}{L_1+L_2}\frac{1-vq}{1-v^2}YQD^2. \tag{2.10b}$$

For example, taking $L_2 = L_1$, $Y = 10^{11}$ N/m^2, $QD^2 = 10^{-3}$, $v = q = 0.3$, one finds that the tensile stress $\sigma^+ = 50$ MPa. We emphasize that the stresses σ^+ and σ^- are valid far away from the electrode edge. The stress field in general must be determined by using the finite element analysis.

2.4. *Computing the stress intensity factor*

Once the stress field is obtained from the finite element calculation, the stress intensity factor can be evaluated by means of the fracture mechanics. Consider a crack-like flaw of length a, taken to be much smaller than the layer thickness, i.e. $a/H \ll 1$. The stress normal to the crack surface, σ_n, induces a stress intensity factor (Tada *et al.*, 1985)

$$K_I = \sqrt{\frac{2}{\pi a}}\int_0^a \sigma_n(x)\sqrt{\frac{x}{a-x}}\,dx. \tag{2.11}$$

We evaluate this integral numerically.

Introduce a dimensionless parameter

$$\alpha = \frac{QD_sY\gamma_s}{E_s} = \frac{Y\gamma_s^2}{\varepsilon E_s^2}, \tag{2.12}$$

which is a material constant that measures the relative magnitude of mechanical and electrical energy. Its mathematical significance can be appreciated as follows. For a ceramic under uniaxial stress σ and electric displacement D, the longitudinal strain γ and electric field E are

$$\gamma = \frac{\sigma}{Y} + QD^2, \quad E = -2QD\sigma + \frac{E_s}{2}\ln\left(\frac{1+D/D_s}{1-D/D_s}\right). \tag{2.13}$$

Normalize the strain by γ_s, the stress by $Y\gamma_s$, the electric displacement by D_s, and the electric field by E_s, so that (2.13) takes a dimensionless form

$$\gamma = \sigma + D^2, \quad E = -2\alpha D\sigma + \frac{1}{2}\ln\left(\frac{1+D}{1-D}\right). \tag{2.14}$$

Similar relation for the multiaxial loading state can also be deduced from (2.4). Consequently, when $\alpha = 0$, the stresses do not affect electric fields. The approximation $\alpha = 0$ has been made in most previous publications, which we will verify in this paper.

The stress intensity factor takes the dimensionless form

$$\frac{K_I}{Y\gamma_s\sqrt{H}} = k\left(\frac{a}{H}, \frac{E_{appl}}{E_s}, \alpha, v, q\right). \tag{2.15}$$

Function k is to be determined from the finite element calculation.

3. SMALL-SCALE SATURATION

This section summarizes the model for an actuator under the small-scale saturation conditions (Suo, 1993; Yang and Suo, 1994; Hao *et al.*, 1996), and compares it with our finite element results.

3.1. *The small-scale saturation model*

When the applied electric field is small compared to the characteristic electric field, $E_{appl} < E_s$, the electric field in the bulk of the actuator is linearly dielectric. The electric field a distance r ahead of the electrode edge is square-root singular

$$E = \frac{K_E}{\sqrt{2\pi r}}. \tag{3.1}$$

The electric field intensity factor K_E depends on the driving voltage and the device geometry, and can be solved from linear dielectric boundary value problems. Linearity and dimensional considerations dictate that the intensity factor should take the form

$$K_E = \Omega E_{appl}\sqrt{H}. \tag{3.2}$$

The dimensionless coefficient $\Omega = \sqrt{2}$ for the present actuator geometry.

Under the small-scale saturation conditions, the electric displacement saturates only within a small cylinder around the electrode edge. The radius of the saturated cylinder is

$$r_s = \frac{1}{2\pi}\left(\frac{K_E}{E_s}\right)^2. \tag{3.3}$$

The linear dielectric solution (3.1) is approximately valid in an annulus with its inner radius larger than the saturated cylinder and outer radius smaller than the individual ceramic layer thickness, i.e. $r_s < r < H$.

Around the electrode edge, the electric field generates an incompatible strain field, which, in its turn, induces a stress field. The high stress field is localized in a region scaled by the saturated cylinder. For a rapidly decaying stress field, the stress intensity factor, K_I, is small for both small and large flaws. Consequently K_I peaks for a flaw of some intermediate size scaled with r_s. The peak value takes the form

$$(K_I)_{max} = \Lambda \frac{Y\gamma_s K_E}{E_s}, \tag{3.4}$$

where the dimensionless number Λ depends on the detail of the material model. Substituting (3.2) into (3.4), one obtains that

$$(K_I)_{max} = \Lambda\Omega \frac{Y\gamma_s E_{appl}\sqrt{H}}{E_s}. \tag{3.5}$$

Consequently, under the small-scale saturation conditions, function k in (2.15) is linear in the loading parameter, E_{appl}/E_s.

No flaws, of any size and location, can grow if $(K_I)_{max} < K_{Ic}$, i.e.

$$\Lambda\Omega \frac{Y\gamma_s E_{appl}\sqrt{H}}{E_s} < K_{Ic}, \tag{3.6}$$

where K_{Ic} is the toughness of the electrostrictive ceramic material. Consequently, everything else being equal, there exists a critical layer thickness, given by

$$H_c = \left(\frac{K_{Ic}E_s}{\Lambda\Omega Y\gamma_s E_{appl}}\right)^2, \tag{3.7}$$

below which no flaw will grow.

The merit of the small-scale saturation approximation can be appreciated as follows. An actuator is made of a complex material with a complex geometry. Under the small-scale saturation conditions, the two complexities, material behavior and geometry effect, can be treated independently. The dimensionless details of a material law only affect the coefficient Λ defined by (3.4), which can be obtained either empirically or by analyzing a material model. The geometry details of the actuator only affect the coefficient Ω defined by (3.2), which can be obtained by analyzing a linear dielectric boundary value problem. The scheme will be particularly useful in evaluating several materials for a common actuator geometry, or several actuator geometries for a common material.

3.2. *Comparison of the finite element calculation with the HGS solution*

We compare the HGS (Hao *et al.*, 1996) solution with the finite element results in this section. In all numerical calculations, we set $\nu = 0.26$, $q = 0.38$, and $L_1 = L_2 = 40H$. We use a small loading level $E_{appl}/E_s = 0.08$ to represent the small-

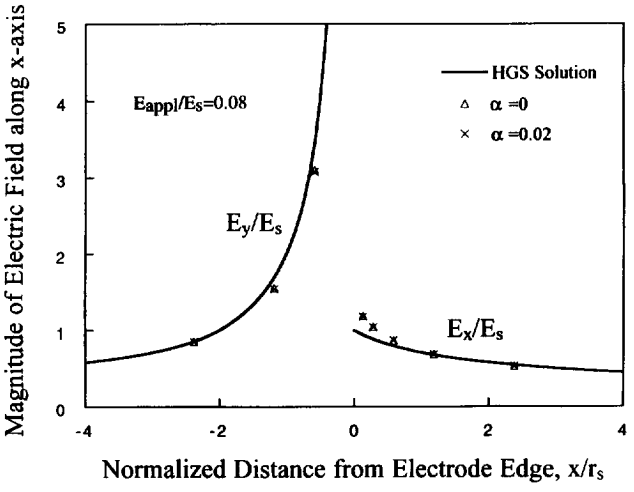

Fig. 5. The electric field distributions along the x-axis under the small-scale saturation conditions.

scale saturation conditions. Figure 5 compares the electric field distribution along the x-axis. The solid line is the HGS solution; the electric field vector lies in the x-direction ahead of the electrode edge, and in the y-direction behind the electrode edge. The finite element results for $\alpha = 0$ and $\alpha = 0.02$ are indicated. As mentioned before, α defined in (2.12) affects the ability of the stress field to influence the electric field. In most existing analytical solutions, this parameter has been set to zero to simplify the analysis. Figure 5 shows that a realistic value $\alpha = 0.02$, does not change the electric field substantially, and both sets of results agree with the HGS solution.

Figure 6 compares the electric displacement distribution. Again, the two cases $\alpha = 0$ and $\alpha = 0.02$ give similar results. The difference between the finite element solutions and the HGS solution is caused by different D–E relations used in the calculations

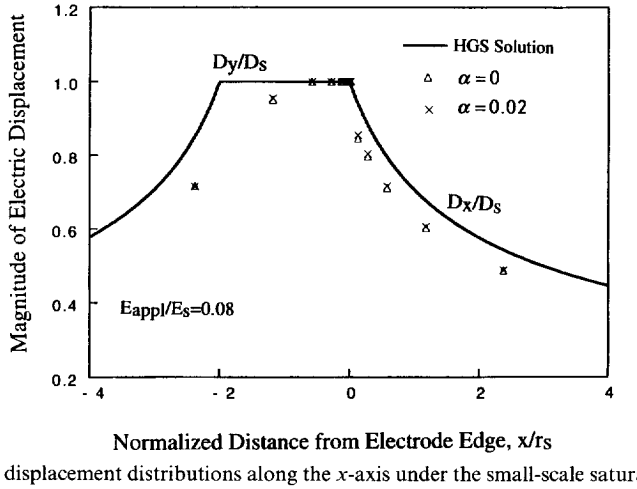

Fig. 6. The electric displacement distributions along the x-axis under the small-scale saturation conditions.

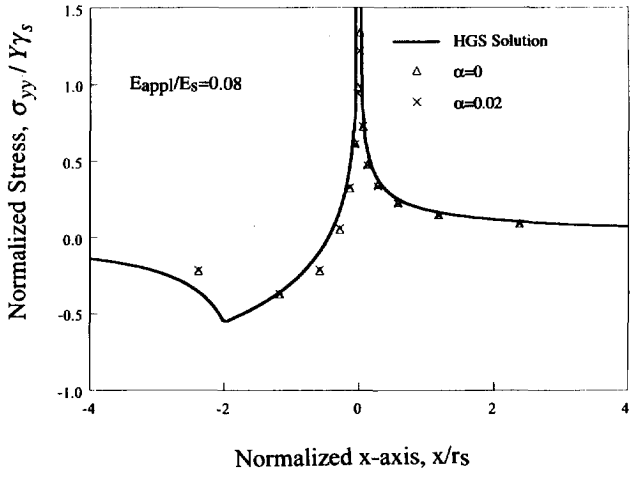

Fig. 7. The normal stress σ_{yy} in the electrode plane and in the plane directly ahead of the electrode edge.

(shown in Fig. 3). This is confirmed by comparing the finite element results with the existing analytical solutions in Appendix B.

Stress distributions along the x-axis are plotted in Figs 7 and 8. The small differences between the HGS solution and the finite element calculation suggest that the stress singularity does not change when using a slightly different D–E relations in Fig. 3. It also suggests that a similar stress intensity factor should be obtained. Consequently, details in the shape of the D–E relation plays little role as far as cracking condition is concerned.

Since the stress contributes negligibly to the electric field. Our finite element calculation under the large-scale saturation conditions will focus on the case $\alpha = 0$.

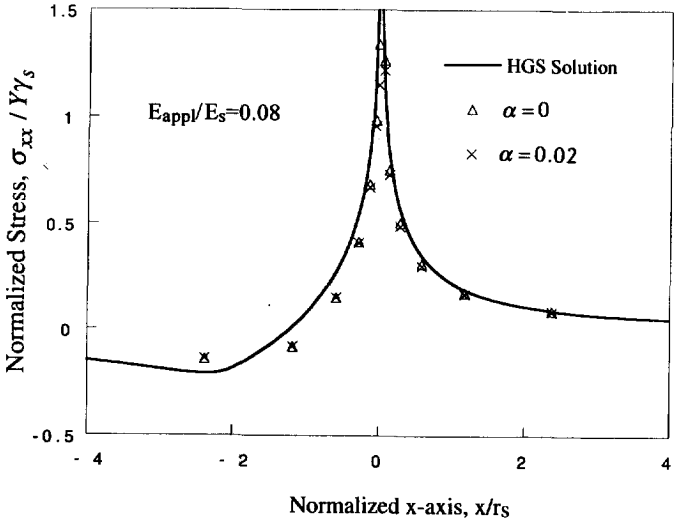

Fig. 8. The normal stress σ_{xx} in the electrode plane and in the plane directly ahead of the electrode edge.

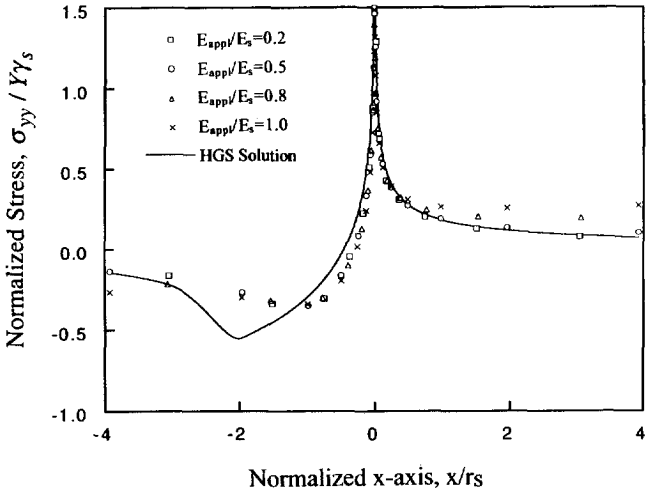

Fig. 9. The normal stress σ_{yy} in the electrode plane and in the plane directly ahead of the electrode edge for different applied electric fields.

4. LARGE-SCALE SATURATION

When the applied electric loading approaches the saturation electric field, the saturation zone size becomes comparable to the layer thickness. The electric field in the ceramic is no longer $r^{-1/2}$ distributed around the electrode edge. Consequently, the electric field intensity factor, K_E, is no longer meaningful, nor is the saturation cylinder radius, r_s. Nevertheless, we can normalize lengths in the similar manner as in the small-scale saturation case by a characteristic length, still written as r_s, but defined by

$$r_s = \frac{HE_{appl}^2}{\pi E_s^2}. \tag{4.1}$$

This definition is motivated by combining (3.2) and (3.3), although neither holds the original physical meaning. Figures 9 and 10 plot the stresses along x-axis at different applied electric fields. The solid lines are the stress distributions under the small-scale conditions. It may be instructive to think of the stress field as a combination of the local logarithmic singular stress field and the global uniform stress field. Near the electrode edge, the stress distributions are similar to those under the small-scale saturation conditions. Far away from the electrode edge, the stress is uniform, compressive behind the edge and tensile ahead of the edge (2.10).

Once the stress field is determined, the stress intensity factor K_I is evaluated for a small flaw from (2.11). The value of K_I depends on the position, orientation and size of the flaw introduced in the calculation. Such information on flaws is in general unavailable, or at the best, imprecise. We assume that the length of the crack-like flaw, a, is on the order of grain diameter, much smaller than the layer thickness, H. To be definite, we place the flaw along the x-axis, with one tip of the flaw at the point behind the electrode edge, where the normal stress changes from compression to

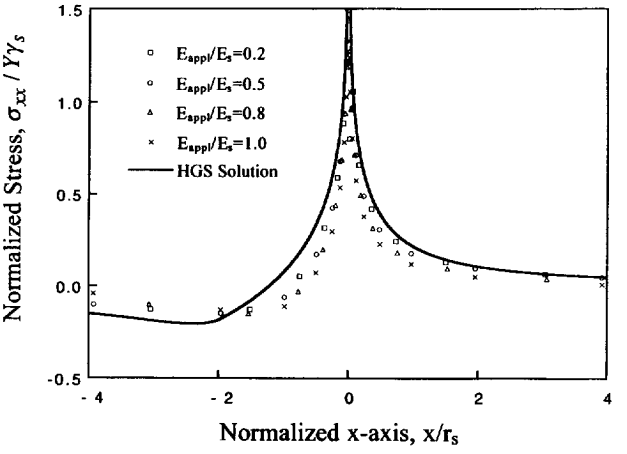

Fig. 10. The normal stress σ_{xx} in the electrode plane and in the plane directly ahead of the electrode edge for different applied electric fields.

tension. Figure 11 shows the calculated stress intensity factor at different applied electric fields. They all peak when the other flaw tip is at the electrode edge, and reaches similar value. The peak value of K_I is written as

$$(K_I)_{max} \cong 0.25 Y\gamma_s \sqrt{2H} \frac{E_{appl}}{E_s}. \tag{4.2}$$

It is noted from Fig. 11 that the prefactor varies with the load level E_{appl}/E_s, but only

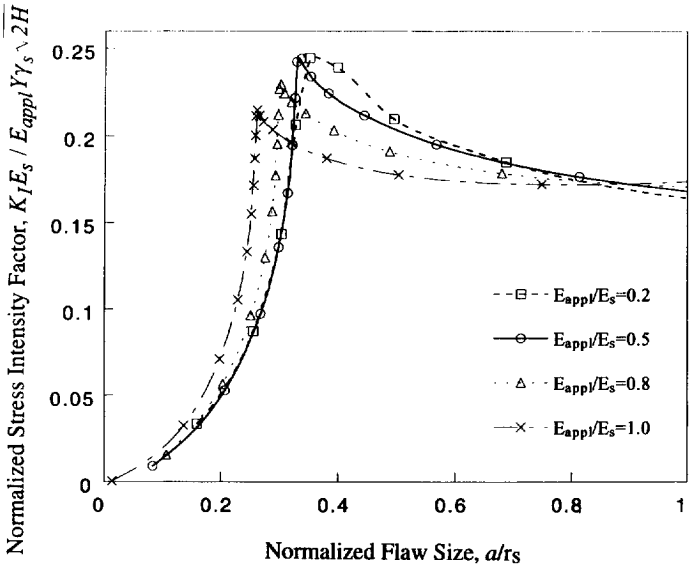

Fig. 11. The stress intensity factor for flaws under different loads.

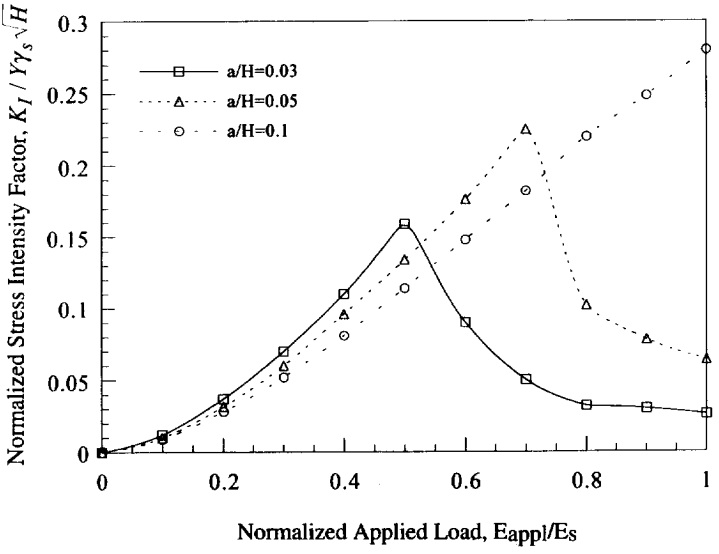

Fig. 12. The stress intensity factor for fixed flaw sizes.

by a small amount. A larger value is chosen to write (4.2) for conservative design. No flaw will grow if $(K_I)_{max} < K_{Ic}$. Equation (4.2) defines a critical layer thickness

$$H_c = 8\left(\frac{K_{Ic}E_s}{Y\gamma_s E_{appl}}\right)^2. \tag{4.3}$$

No flaw will grow if every individual layer of the actuator is thinner than H_c. The form of the above expression is identical to the small-scale saturation approximation (3.7). The prefactor in (4.3), however, depends on the load level E_{appl}/E_s. The value used in (4.3) belongs to $E_{appl}/E_s = 0.2$, which serves as a conservative approximation, judging from Fig. 11.

The above cracking condition is derived under the assumption that small flaws are available in a size range, and the flaw that maximizes K_I is critical. Consequently, the cracking condition so derived does not depend on the flaw size. If, however, the flaw size a is known from processing, a different cracking condition can be formulated. Figure 12 shows crack driving force for three flaw sizes as a function of applied electric loads. For large flaws, K_I keeps increasing as the applied loading increases. For small flaws, K_I peaks at a certain applied load. The peak values are basically the same as one obtained from Fig. 11. Based on this behavior, we construct a maximum crack driving force versus normalized flaw sized curve in Fig. 13. Below this curve, flaws cannot grow at any electrical loads.

5. CONCLUDING REMARKS

The finite element calculation indicates that the crack nucleation condition deduced from the small-scale saturation is still approximately valid when the applied electric

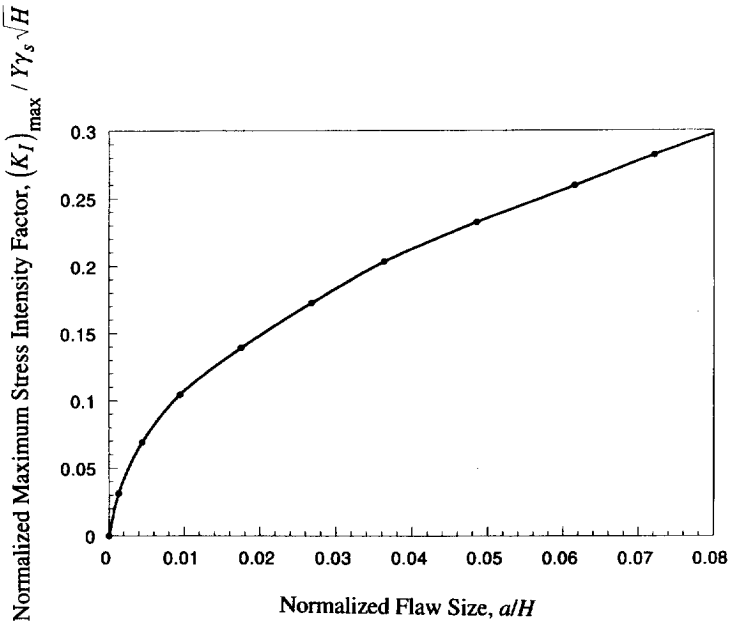

Fig. 13. The maximum stress intensity factor.

field approaches the saturation field. More accurate cracking conditions under the large-scale saturation conditions can also be obtained in similar forms, but with different numerical coefficients. Stress induced by electrostriction consists of two parts: a uniform stress induced by the overall strain mismatch far behind and far ahead of the electrode edge, and a nonuniform stress induced by the electric field concentration near the electrode end. For the particular geometry we have analyzed in the paper, the second part plays the dominant role in crack nucleation. For a typical actuator, where the gap between the internal electrode edge and the actuator end (L_1 in Fig. 4) is comparable to the layer thickness H, a further study on actuator geometry dependence of the cracking criterion is necessary.

ACKNOWLEDGEMENT

This work is supported by NSF through grant MSS-9258115, and by ONR through contract N00014-93-1-0110.

REFERENCES

Aburatani, H., Harada, S., Uchino, K. and Furuta, A. (1994) Destruction mechanism of ceramic multilayer actuators. *Japanese J. Appl. Phys.* **33,** 3091–3094.

Cao, H. C. and Evans, A. G. (1993) Nonlinear deformation of ferroelectric ceramics. *J. Am. Ceram. Soc.* **76,** 890–896.

Furuta, A. and Uchino, K. (1993) Dynamic observation of crack propagation in piezoelectric multilayer actuators. *J. Am. Ceram. Soc.* **76,** 1615–1617.
Gong, X. (1994) Stresses near the end of an internal electrode in multilayer electrostrictive ceramic actuators. *Mater. Res. Soc. Symp. Proc.* **360,** 83–88.
Gong, X. (1995) A finite element solution of failures in capacitor-type multilayer ferroelectric ceramic actuators. *Adaptive Material Systems, ASME*, 57–63.
Hom, C. L. and Shankar, N. (1994) A fully coupled constitutive model for electrostrictive ceramic materials. *J. Intelligence Mater. Sys. Struct.* **5,** 795–801.
Hom, C. L. and Shankar, N. (1995) A finite element method for electrostrictive ceramic devices. *Int. J. Solids Struct.*, in press.
Hao, T. H., Gong, X. and Suo, Z. (1996) Fracture mechanics for the design of ceramic multilayer actuators. *J. Mech. Phys. Solids* **44,** 23–48.
Lynch, C. S. (1995) The effect of uniaxial stress on the electro-mechanical response of 8/65/35 PLZT. Submitted to *Acta Metall. Mater.*
Lynch, C. S., Yang, W., Collier, L., Suo, Z. and McMeeking, R. M. (1994) Electric field induced cracking in ferroelectric ceramics. *Ferroelectrics* **166,** 11–30.
Rice, J. R. (1967) Stresses due to a sharp notch in a work-hardening elastic-plastic material loaded by longitudinal shear. *J. Appl. Mech.* **34,** 287–298.
Rogers, C. A. (1995) Intelligent materials. *Scientific American*, September Issue, 154–157.
Schneider, G. A., Rostek, A., Zickgraf, B. and Aldinger, F. (1994) Crack growth in ferroelectric ceramics under mechanical and electrical loading. *Proc. 4th, Int. Conf. Elect. Ceram. & Appl.* 1211–1216.
Suo, Z. (1991) Mechanics concepts for failure in ferroelectric ceramics. *Smart Structures and Materials* (ed. A. V. Srinvasan), pp. 1–6. ASME, New York.
Suo, Z. (1993) Models for breakdown resistant dielectric and ferroelectric ceramics. *J. Mech. Phys. Solids* **41,** 1155–1176.
Tada, H., Paris, P. C. and Irwin, G. R. (1985) *The Stress Analysis of Cracks Handbook*. Del Research, St. Louis, MO.
Uchino, K. (1993) Ceramic actuators: principles and applications. *MRS Bulletin*, April Issue, 42–48.
Uchino, K. and Nomura, S. (1983) Electrostriction in PZT-family antiferroelectrics. *Ferroelectrics* **50,** 191–196.
Winzer, S. R., Shankar, N. and Ritter, A. P. (1989) Designing cofired multilayer electrostrictive actuators for reliability. *J. Am. Ceram. Soc.* **72,** 2246–2257.
Yang, W. and Suo, Z. (1994) Cracking in ceramic actuators caused by electrostriction. *J. Mech. Phys. Solids* **42,** 649–663.
Yoshikawa, S. and Shrout, T. (1993) Multilayer piezoelectric actuators: structures and reliability. American Institute of Aeronautics and Astronauts (AIAA)-93-1711-CP.
Zienkiewicz, O. C. (1977) *The Finite Element Method.* McGraw-Hill Book Company.

APPENDIX A: FINITE ELEMENT METHOD FOR NONLINEAR ELECTROSTRICTIVE CERAMICS

We use eight-node quadratic isoparametric elements (Zienkiewicz, 1977). Divide the physical plane x–y into many (possibly curved) quadrilaterals, and map every element to a square with side length 2 in the calculation plane ξ–η according to

$$x = \sum_{i=1}^{8} x_i N_i(\xi, \eta), \quad y = \sum_{i=1}^{8} y_i N_i(\xi, \eta), \tag{A.1}$$

where (x_i, y_i) are the nodal position vectors, and $N_i(\xi, \eta)$ are the interpolation functions. Denote the nodal values of the displacements and electric potential by u_i, v_i, ϕ_i. Approximate the field $u(x, y)$, $v(x, y)$, and $\phi(x, y)$ within an element in the same way as the position vectors, namely

$$u(x,y) = \sum_{i=1}^{8} u_i N_i(\xi,\eta), \quad v(x,y) = \sum_{i=1}^{8} v_i N_i(\xi,\eta), \quad \phi(x,y) = \sum_{i=1}^{8} \phi_i N_i(\xi,\eta). \tag{A.2}$$

Write all the nodal values of u, v, and ϕ on the mesh by a column, $\mathbf{a}$, and assemble the above interpolation in matrix form

$$\begin{bmatrix} u(x,y) \\ v(x,y) \\ \phi(x,y) \end{bmatrix} = \mathbf{N}\mathbf{a}, \tag{A.3}$$

where $\mathbf{N}$ contains the interpolation functions for all the nodes of the entire mesh.

The basic field equations in Section 2 can be written as a weak statement

$$\int(\sigma_{ij}\,\delta\gamma_{ij} - D_i\,\delta E_i)\,\mathrm{d}v = \int(t_i\,\delta u_i - \omega\,\delta\phi)\,\mathrm{d}s. \tag{A.4}$$

Here $\delta(\,)$ indicates small variations. Denote

$$\mathbf{\Sigma} = \begin{bmatrix} \sigma_x \\ \sigma_y \\ \tau_{xy} \\ D_x \\ D_y \end{bmatrix}, \quad \mathbf{\Gamma} = \begin{bmatrix} \gamma_x \\ \gamma_y \\ 2\gamma_{xy} \\ -E_x \\ -E_y \end{bmatrix}, \quad \mathbf{T} = \begin{bmatrix} t_x^0 \\ t_y^0 \\ -\omega^0 \end{bmatrix}. \tag{A.5}$$

Here $\mathbf{t}^0$ is the traction prescribed on part of the boundary S_t, and ω^0 is the charge per unit area prescribed on part of the boundary S_ω. Taking gradients of the displacements and the electric potential according to (A.3) and (2.1), one obtains that

$$\delta\mathbf{\Gamma} = \mathbf{B}\,\delta\mathbf{a}, \tag{A.6}$$

where $\mathbf{B}$ is the matrix resulting from the differentiation. In the discretized form (A.4) becomes

$$\delta\mathbf{a}^{\mathrm{T}} \int_v \mathbf{B}^{\mathrm{T}}\mathbf{\Sigma}\,\mathrm{d}v = \delta\mathbf{a}^{\mathrm{T}} \int_{S_t + S_\omega} \mathbf{N}^{\mathrm{T}}\mathbf{T}\,\mathrm{d}S. \tag{A.7}$$

The superscript T stands for the transpose of a matrix. Since (A.7) holds true for arbitrarily chosen $\delta\mathbf{a}$, one concludes that

$$\int_v \mathbf{B}^{\mathrm{T}}\mathbf{\Sigma}\,\mathrm{d}v = \int_{S_t + S_\omega} \mathbf{N}^{\mathrm{T}}\mathbf{T}\,\mathrm{d}S. \tag{A.8}$$

Notice $\mathbf{\Sigma}$ is a function of $\mathbf{\Gamma}$, and therefore a function of $\mathbf{a}$. Equation (A.8) is a set of nonlinear equations for a nodal variables $\mathbf{a}$. They are solved incrementally by linear equations

$$\mathbf{K}\,\Delta\mathbf{a} = \Delta\lambda\mathbf{R}. \tag{A.9}$$

Here $\Delta\mathbf{a}$ is the increment, $\Delta\lambda$ is a parameter that controls the loading increment, $\mathbf{K}$ is the tangential stiffness matrix

$$\mathbf{K} = \int_v \mathbf{B}^{\mathrm{T}}\mathbf{C}^{-1}\mathbf{B}\,\mathrm{d}v, \tag{A.10}$$

and $\mathbf{R}$ is the equivalent load

$$\mathbf{R} = \int_{S_t + S_\omega} \mathbf{N}^{\mathrm{T}}\mathbf{T}\,\mathrm{d}S. \tag{A.11}$$

The matrix $\mathbf{C}$ contains the differential coefficients of the constitutive equations, namely

$$d\Gamma = \mathbf{C}\, d\Sigma. \tag{A.12}$$

The matrix $\mathbf{C}$ is symmetric, but in general not positive-definite.

APPENDIX B: ELECTRIC FIELD NEAR ELECTRODE EDGE

When the effect of stress on the electric field is negligible, the governing equations for the electric field around an electrode edge take the same form as the governing equations for the

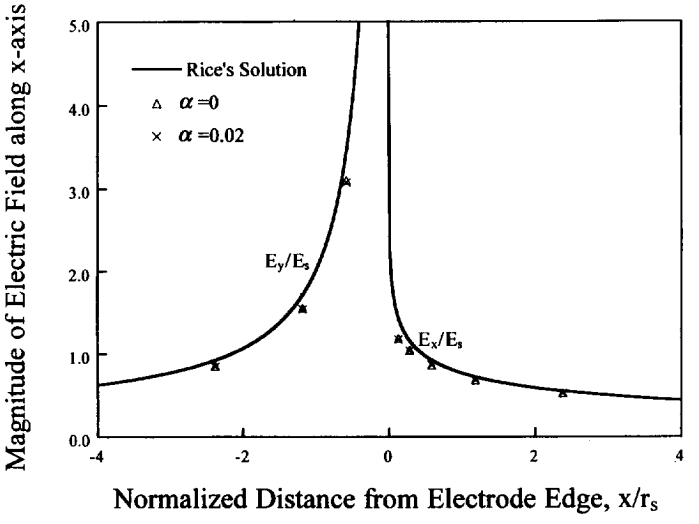

Fig. B1. Comparison of the electric field distribution along the x-axis between finite element solution and the analytic solution.

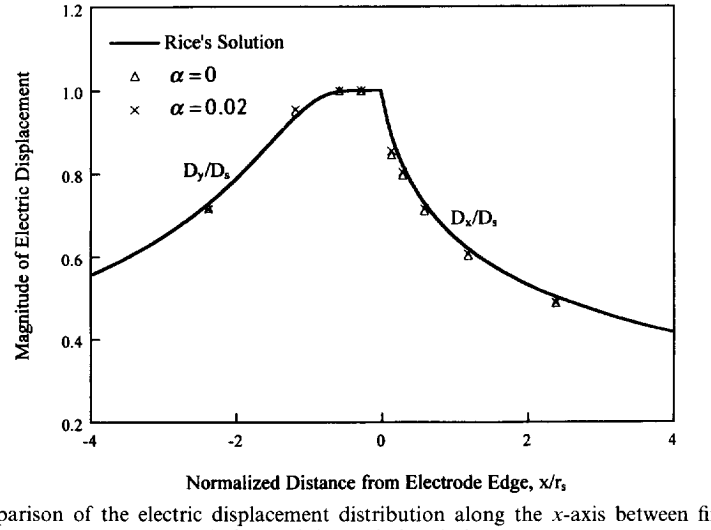

Fig. B2. Comparison of the electric displacement distribution along the x-axis between finite element solution and the analytic solution.

stress field around a mode III crack tip. We now interpret Rice's (1967) solution of a mode III crack in a nonlinearly elastic solid for an electrode in a nonlinearly dielectric solid. Let D, E be the magnitude of electric displacement and electric field, φ be the angle between the direction of the electric field and the x-direction, measured positive counterclockwise. Write

$$X(E) = \frac{K_E^2}{2\pi E_s^2}\left[2\int_E^\infty \frac{du}{u^2 D(u)} - \frac{1}{ED(E)}\right], \tag{B.1}$$

$$R(E) = \frac{K_E^2}{2\pi E_s^2 ED(E)}, \tag{B.2}$$

where K_E is the electric field intensity factor of an asymptotic approach to the linear D–E interaction. For a given electric field magnitude E, the position coordinates are

$$x = -X(E) - R(E)\cos 2\varphi, \quad y = R(E)\sin 2\varphi. \tag{B.3}$$

This solution for the dielectric law (2.5) is plotted and compared with the finite element solution for small scale saturation in Fig. A1 and Fig. A2.